

1 **Probing the extreme planetary atmosphere of** 2 **WASP-12b**

3 *Mark Swain, Jet Propulsion Laboratory, California Institute of Technology, 4800 Oak Grove Drive,*
4 *Pasadena, CA 91109, USA*

5 *Pieter Deroo, Jet Propulsion Laboratory, California Institute of Technology, 4800 Oak Grove Drive,*
6 *Pasadena, CA 91109, USA*

7 *Giovanna Tinetti, University College London, Department of Physics and Astronomy, Gower Street,*
8 *London WC1E 6BT, UK*

9 *Morgan Hollis, University College London, Department of Physics and Astronomy, Gower Street, London*
10 *WC1E 6BT, UK*

11 *Marcell Tessenyi, University College London, Department of Physics and Astronomy, Gower Street,*
12 *London WC1E 6BT, UK*

13 *Michael Line, California Institute of Technology, Pasadena, CA 91106, USA*

14 *Hajime Kawahara, Department of Physics, Tokyo Metropolitan University, Hachioji, Tokyo 192-0397,*
15 *Japan*

16 *Yuka Fujii, Department of Physics, The University of Tokyo, Tokyo 113-0033, Japan*

17 *Adam P. Showman, Department of Planetary Sciences and Lunar and Planetary Laboratory, The*
18 *University of Arizona, 1629 University Blvd., Tucson, AZ 85721, USA*

19 *Sergey N. Yurchenko, University College London, Department of Physics and Astronomy, Gower Street,*
20 *London WC1E 6BT, UK*

21 **Abstract**

22 We report near-infrared measurements of the terminator region transmission spectrum
23 and dayside emission spectrum of the exoplanet WASP-12b obtained using the HST
24 WFC3 instrument. The disk-average dayside brightness temperature averages about
25 2900 K, peaking to 3200 K around 1.46 μm . We modeled a range of atmospheric cases
26 for both the emission and transmission spectrum and confirm the recent finding by
27 Crossfield et al. (2012b) that there is no evidence for $\text{C/O} > 1$ in the atmosphere of
28 WASP-12b. Assuming a physically plausible atmosphere, we find evidence that the
29 presence of a number of molecules is consistent with the data, but the justification for
30 inclusion of these opacity sources based on the Bayesian Information Criterion (BIC) is
31 marginal. We also find the near-infrared primary eclipse light curve is consistent with
32 small amounts of prolate distortion. As part of the calibration effort for these data, we

33 conducted a detailed study of instrument systematics using 65 orbits of WFC3-IR grims
34 observations. The instrument systematics are dominated by detector-related affects,
35 which vary significantly depending on the detector readout mode. The 256×256 subarray
36 observations of WASP-12 produced spectral measurements within 15% of the photon-
37 noise limit using a simple calibration approach. Residual systematics are estimated to be
38 ≤ 70 parts per million.

39 **1. Introduction**

40 Among the more than 700 currently confirmed exoplanets, WASP-12b stands out as
41 exceptional. This transiting gas giant, with a mass of 1.39 MJ and a radius of 1.83 RJ,
42 orbits a 6300-K G star with a period of 1.09 days, resulting in an extraordinary level of
43 insolation and, thus, extreme atmospheric heating (Hebb et al. 2009). Given the close
44 proximity to the stellar primary, this system presents an opportunity to study a planetary
45 atmosphere in a unique environment. The combination of the unusual nature of this
46 system, the relatively bright stellar primary, and the system orientation, which provides
47 both primary and secondary eclipse events, has made this target one of the more
48 extensively observed exoplanet systems. Analysis of these observations has led to several
49 noteworthy results that underscore the unique nature of this planet. For example,
50 WASP-12b is inflated to an unusual degree that could imply significant internal heating
51 (Ibgui et al. 2010). The atmosphere is likely extended, and the planet may be losing
52 substantial mass through Roche lobe overflow (Li et al. 2010); there is also evidence
53 supporting the presence of a magnetospheric bow shock (Llama et al. 2011). The planet
54 has been proposed to be carbon rich, with a $C/O \geq 1$ (Madhusudhan et al. 2011a), a
55 condition that may reduce TiO and VO abundances (Madhusadhan et al. 2011b).

56 Recently, Spitzer measurements were reported that show a large-amplitude thermal phase
57 curve with a significant phase offset at 3.6 μm (Cowan et al. 2012).

58 High-precision, near-infrared spectroscopy has the potential to provide additional
59 constraints that complement the exiting measurements of WASP-12b. Previous near-
60 infrared spectroscopic observations with Hubble Space Telescope (HST) have detected
61 molecules such as H_2O , CO_2 , CH_4 , and CO in three hot-Jovian-type planets (Swain et al.
62 2008, 2009a, 2009b, Tinetti et al. 2010) and produced important constraints on the
63 atmosphere of a hot-Neptune (Pont et al. 2009) and Super Earth (Berta et al. 2011). The
64 need for near-infrared measurements of WASP-12b has been partially addressed with
65 ground-based photometry (Croll et al. 2011, Zhao et al. 2012) and spectroscopy
66 (Crossfield et al. 2012a), although the precision of these observations was not sufficient
67 to detect molecular features. Here we report high-precision, near-infrared spectroscopy
68 measurements obtained with the HST.

69 **2. Methods: Observations and Data Calibration**

70 **2.1 Observations**

71 We observed the WASP-12b system using the WFC3 instrument with the G141 grism,
72 which provides spectral coverage from 1.1 to 1.7 μm with a spectral resolution of $R=300$
73 at 1.38 μm . The observations reported here consist of two HST visits, each with five
74 consecutive orbits, timed to measure a primary and secondary eclipse event (see Figure 1).
75 For both events, the observations track the system light curve from pre-ingress to post-
76 egress to provide a spectrophotometric baseline from which the eclipse depth can be
77 measured. The primary eclipse (transit), when the planet blocks some of the light from
78 the stellar primary, probes the transmission spectrum of the planet's terminator region
79 atmosphere. The secondary eclipse (occultation), when the planet passes behind the

80 stellar primary, probes the emission spectrum of the planet's dayside atmosphere. For
81 these observations, the primary and secondary eclipse measurements were timed to be
82 separated by the minimum possible time feasible with HST with the objective of
83 minimizing any effects due to temporal changes in the exoplanet atmosphere or parent
84 star. After both the primary and secondary eclipse observation sequence, we observed a
85 calibrator star, HD 258439, with two consecutive orbits. Detector-specific configuration
86 information, such as integration time and subarray size, is contained in Table 1. Our
87 choices for the detector readout mode maximized the instrument efficiency and avoided
88 the WFC3 overheads that can reduce significantly the instrument efficiency when
89 observing relatively bright objects, such as transiting exoplanet systems.

90 The near-infrared spectral signatures of transiting exoplanets, for both transmission
91 and emission measurements, require precision measurements; consequently, the potential
92 impact of instrument systematic errors must be considered. A purpose-built instrument,
93 which would eliminate many of these problems, does not yet exist, and the field has to
94 make the best of the instruments available. This underscores the need for careful
95 investigation and a thorough understanding of instrument characteristics. This is best
96 done by a systematic analysis of a large amount of data so that characteristic instrument
97 behavior patterns can be identified. WFC3 is relatively new and an investigation of the
98 instrument is especially timely.

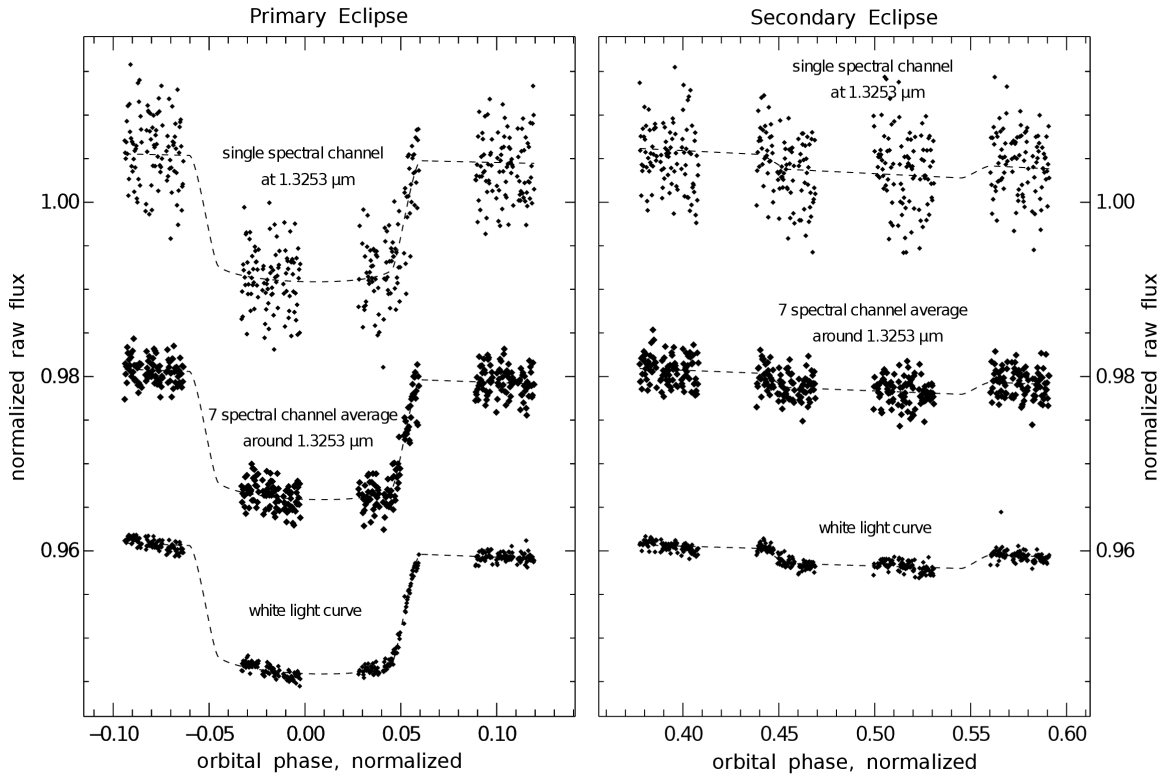


Figure 1: The WFC3 observation of the WASP-12b primary eclipse (left) and secondary eclipse (right) showing spectral and broad-band light curves as a function of orbital phase. The light curves are based on .flt data (see text for discussion) for orbits 2-5 and have been vertically offset for display clarity. A best fit linear detrending combined with a light curve model are shown (dashed); no data filtering or decorrelation has been applied. The gaps in the data are due to Earth occultations.

99 2.2 WFC3 Systematics

100 Here we report on a detailed investigation of WFC3 instrument systematic errors
 101 using a large amount of archival data. Readers primarily interested in the science results
 102 can skip to Section 2.3.

103 To characterize the instrument, we analyzed 65 orbits of archive data covering 10
 104 objects, using the data from individual non-destructive reads to mitigate the complicating
 105 factors of the range of target brightness and the fact that some groups appear to have over

106 exposed their targets. We probed the detector system by analysis of both the standard
107 pipeline output and lower level data products (both “_raw” and “_ima” archive file types).
108 We searched for a measurement dependence on the instrument optical state by
109 constructing estimates for focus, spectrum position, and spectrum rotation. The spectral
110 extraction and determination of optical state parameters was performed as described in
111 Swain et al. 2009b. In contrast to NICMOS, in which optical state parameters such as
112 focus and spectral position produced large instrument systematics, we find that the WFC3
113 instrument optical state changes, while measurable, produce negligible systematic
114 changes in the measured spectroscopic flux density. In this regard, we confirm previous
115 findings (Berta et al. 2011). We attribute this independence of the measured flux density
116 on instrument optical state parameters as likely due to a high level of uniformity in the
117 instrument focal plane array. Thus, small changes in the illumination function do not
118 produce significant changes in the measured flux density. Another area where we see a
119 marked improvement over NICMOS is that, with WFC3, there is less “spacecraft settling”
120 at the beginning of the observations.

121 Analysis of the 65 orbits, using a consistent approach, reveals the way in which the
122 WFC3 detector system responds to light changes with time in the 512×512 and 128×128
123 subarray modes; these changes can occur on intra-orbit, inter-orbit, or visit-to-visit time
124 scales (for details, see Figures 2, 3, 4 and 5 and the Supplementary Information).
125 Importantly, these changes are only clearly detectable by analyzing the individual non-
126 destructive reads as the detector is sampled up the ramp during an integration time. There
127 are also significant, systematic changes in the average detector linearity relation due to
128 over-exposure of the array (see Figure 5). Our results are consistent with the WFC3

129 Instrument Handbook, where the full-well saturation level of the IR channel for science
130 observations is given as $\sim 40,000$ DN or 100,000 electrons for the default gain of 2.5
131 electrons per DN. Analysis of the highly saturated HD 189733b observations shows that
132 physical full-well capacity is between $\sim 57,000$ and $\sim 60,000$, depending on the pixel.

133 Detector-system-related instrument systematics, if not correctly accounted for, have
134 the potential to compromise measurement of an exoplanet spectrum. The 256×256
135 subarray data we analyzed suffered less from most of these problems, which implies the
136 root cause may be connected to the array readout process and not to fundamental detector
137 physics. However, until the root cause of changes in the detector response to light are
138 understood, we caution that any exoplanet spectroscopy observations need to be analyzed
139 at the level of individual non-destructive reads. Our findings summarizing the readout
140 mode and type/extent of detector system systematic are summarized in Table 1 and
141 Figure 2.

Table 1: *The WFC3 IR-grism exoplanet spectroscopy program objects and data sets analyzed for systematic errors using the ratio of the measurement variance to the photon noise; results are shown for the best out of eclipse orbit. We characterized the extent of the ramp effect with the same method. Detailed difference in the systematic errors, present in some data sets, are visible in the N_{samp} relative flux 1.2-series figures in the Supplementary Material.*

WFC3 IR-grism data analyzed for instrument systematics									
Observational Parameters							Detector Systematics		
source	yy-mm-dd	Orbits	H mag.	Spectral Type	Integration time (sec)	ND reads	Subarray	best orbit	Ramp
WASP-12	11-04-11	5	10.23	G0	7.35	3	256	1.3	3.7
WASP-12	11-04-11	5	10.23	G0	7.35	3	256	1.4	3.1
WASP-12	11-04-11	2	10.23	G0	7.35	3	256	1.3	3.9
HD 258439	11-04-11	2	9.11	A0V	2.24	9	256	1.9	0.5
HD 258439	11-04-11	2	9.11	A0V	2.24	9	256	2.5	0.0
HD 258439	11-04-11	2	9.11	A0V	2.24	9	256	1.8	0.0
COROT-2	10-10-18	4	10.44	G7V	21.65	4	128	5.8	4.0
WASP-4	10-11-25	5	10.84	G8	36.01	7	128	2.5	6.7
WASP-4	10-11-25	5	10.84	G8	36.01	7	128	3.1	6.6
GJ1214	10-10-08	4	9.09	M4	5.95	7	512	5.6	4.3
HAT-P-7	10-09-29	5	9.34	F	7.65	9	512	9.2	8.5
HAT-13	10-09-08	5	9.06	G4	7.65	9	512	12.6	6.0
TRES-2	10-10-09	4	9.92	GOV	12.75	15	512	8.3	4.1
TRES-4	10-11-23	5	10.35	F	12.75	16	512	4.8	0.1
HD 189733	10-11-10	5	5.6	K1	0.23	2	128	Highly saturated	
HD 189733	10-09-04	5	5.6	K1	0.23	2	128	Highly saturated	

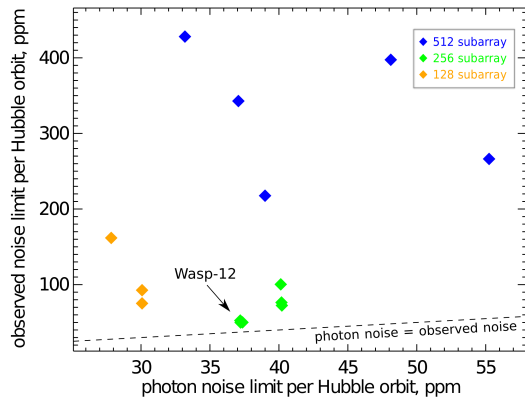


Figure 2: A comparison of detector subarray performance showing the superior performance of the 256×256 subarray. These results are based on comparing the standard deviation of the best orbit for each data set to the photon noise.

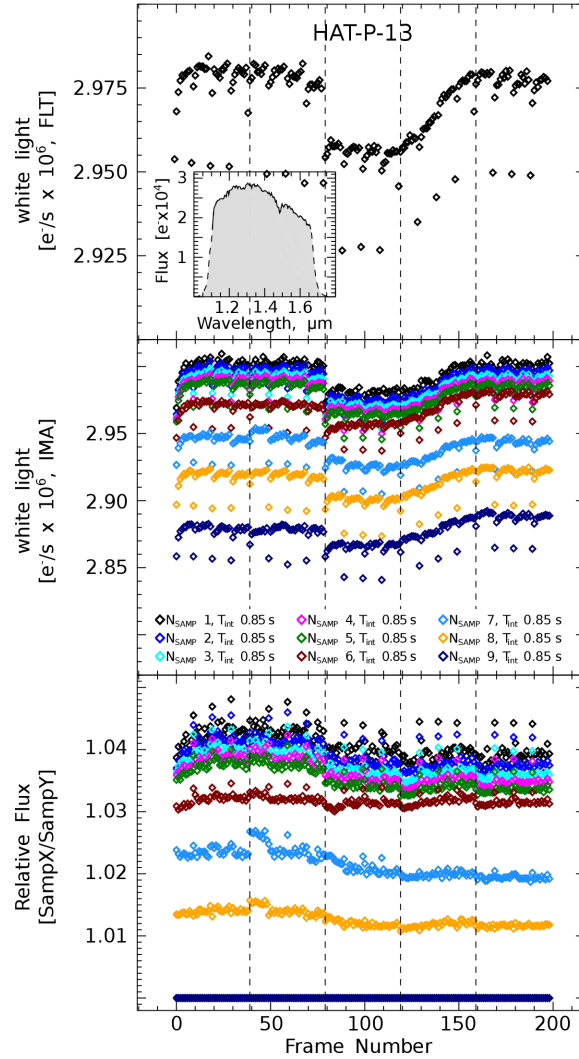


Figure 3: An example of one of the standard diagnostics produced for each object in the 65 orbit data set used for assessing WFC3 systematics, with vertical dashed lines indicating a break between consecutive orbits. (Top) Broadband flux time series based on the standard pipeline data reduction. (Middle) Broadband flux time series based on individual non-destructive reads. The integration time for each non-destructive read is T_{int} in seconds. (Bottom) Normalized non-destructive read time series; these provide an easy way to visualize changes in detector functionality on all time scales.

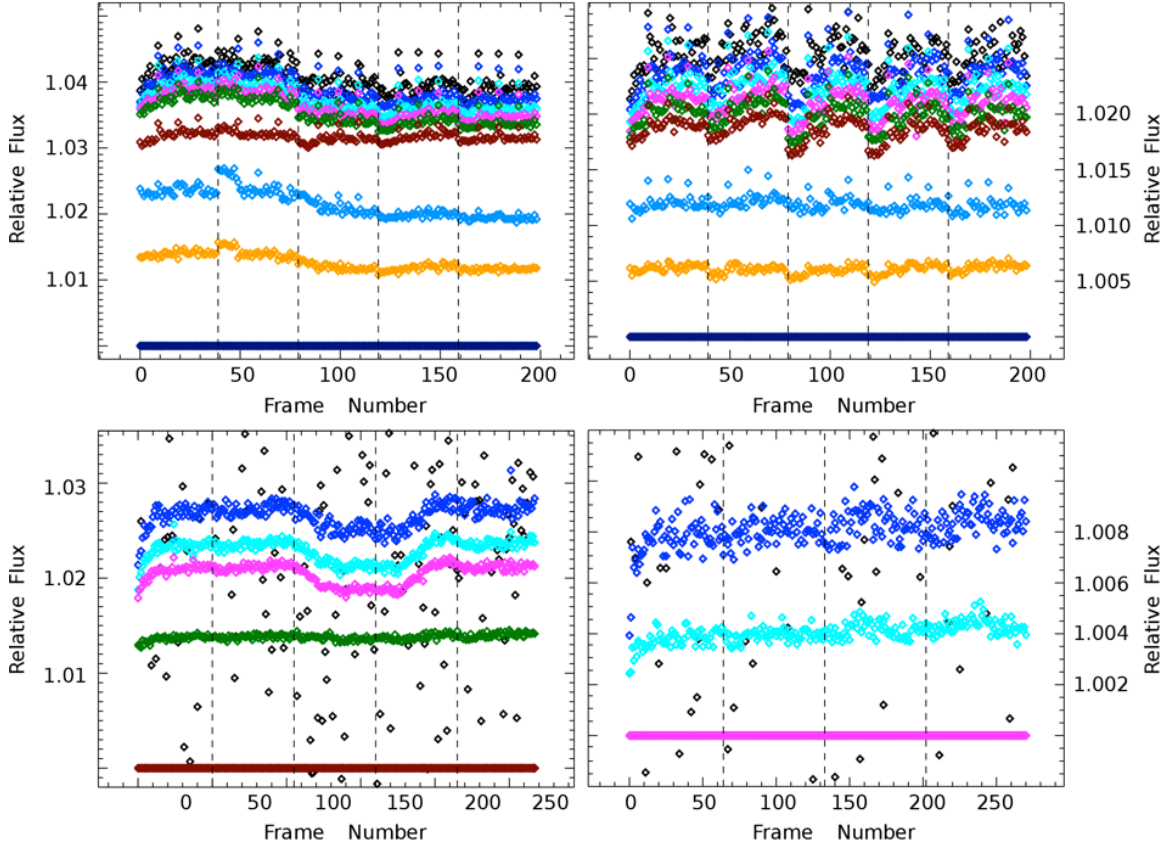


Figure 4: Normalized N_{samp} time series showing undesirable detector functionality changes (top and lower left) that could affect an exoplanet measurement. Each sample-up-the-ramp read is divided by the last read in the series. In the absence of detector-related systematics, the different time series should be constant. Instead, each of the above examples displays inter-orbit and/or intra-orbit systematics. This diagnostic is most useful in observations with several non-destructive reads (i.e., $NSAMP > 3$). The exoplanet systems in these examples (clockwise from top left) are HAT-P-13 (512×512 subarray), HAT-P-7 (512×512 subarray), Corot-1 (128×128 subarray), and WASP-4 (128×128 subarray).

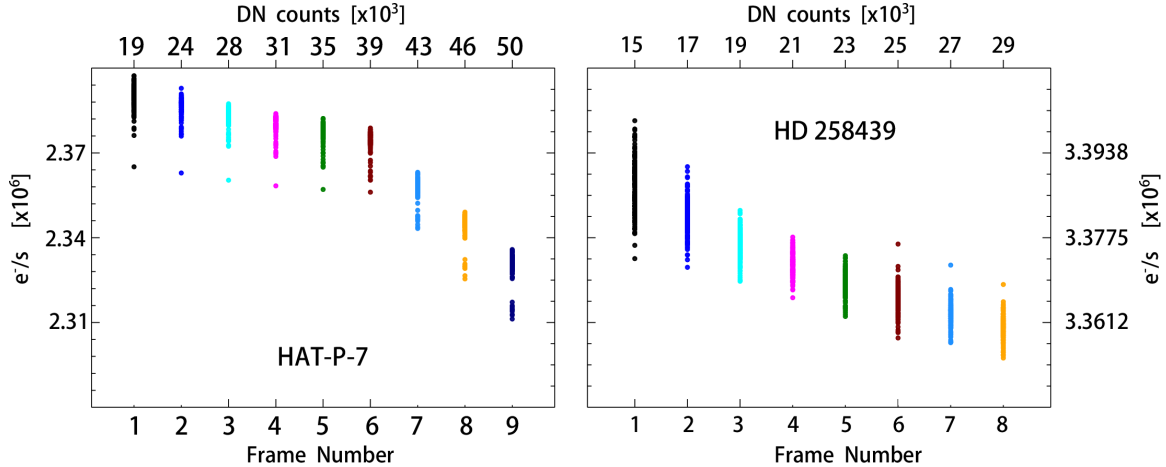


Figure 5: The derivative of the detector linearity relation for two sources. We found a characteristic “knee” in this diagnostic when the detector well is filled beyond ~40,000 DN. A complete set of these figures is in the Supplementary information.

142 In a recent analysis of WFC3-IR spectroscopy of the exoplanet GJ 1214b, observed in
 143 the 512×512 subarray mode, Berta et al. (2011) reported a “ramp” effect of increased flux
 144 measured in sequential integrations. Clarification is needed because the terminology in
 145 the literature is potentially confusing; the ramp in flux measured with sequential
 146 integrations reported by Berta et al. (2011) is undesirable and completely different from
 147 the ramp in flux measured by consecutive nondestructive reads occurring during an
 148 integration (frequently termed “sampling up the ramp”). We find that the extent of ramp
 149 effect seen by Berta et al. (2011) in the flux time series is strongly correlated to the length
 150 of time needed for a WFC3 buffer dump. The buffer dump operation lasts between 8 and
 151 9 minutes in 512×512 subarray mode, about 3 minutes in 256×256 subarray mode, and 1
 152 minute or less in 128×128 mode. In the case of the 128×128 and 256×256 subarray
 153 modes, the ramp effect is minimal and, in some cases, may not be present. In contrast, the
 154 512×512 subarray mode ramp feature is larger and more persistent in that it establishes a
 155 trend that dominates the data for each block of measurements. During the camera buffer

156 dump operation, the array is operated in a charge-flush mode. This charge flush mode
157 interacts with the 512×512 subarray in a way that is qualitatively and quantitatively
158 different from the 256×256 or 128×128 subarray modes. When Earth occultations
159 prevent observing the source, the array is again operated in charge-flush mode. The effect
160 of this is that there is a ramp present at the beginning of the measurements for each orbit.
161 In the case of the 256×256 and 128×128 subarray modes, this ramp is very short, lasting
162 only one or two samples; in the case of the 512×512 subarray modes, the ramp can
163 continue until the next buffer dump and, for the 512×512 subarray, the effect of ~ 45 min.
164 of charge flush array operation is similar to the effect of ~ 9 min of charge-flush operation.

165 For future observations of exoplanet systems with WFC3, we suggest the following
166 guidelines.

- 167 1. Avoid the use of the 512×512 subarray mode.
- 168 2. Set the integration time so that the detector receives no more than $\sim 40,000$ DN
169 before resetting.
- 170 3. Use a small number of samples up the ramp (for non-spatial scanning
171 observations).
- 172 4. Work directly with the individual non-destructive read samples in the data
173 reduction process.

174 Recommendation (1) avoids the intra/inter orbit variations in detector function that
175 are seen in the 512×512 subarray mode, improves instrument overhead, and reduces the
176 ramp effect. Recommendation (2) avoids the changes in detector function that can occur
177 during an integration. Recommendation (3) maximizes the instrument throughput by
178 delaying triggering a buffer dump due to the limit imposed by the file index counter.

179 Recommendation number (4) provides a direct way to assess any changes in detector
180 functionality.

181 **2.3 Extracting the Spectra of WASP-12b**

182 Due to operation in the 256×256 subarray mode, WASP-12 observations are of such
183 high quality that a simple method can be used to determine the eclipse depth. In the case
184 of both the primary and secondary eclipse, the eclipse light curves are constructed from
185 the Nsamp=2 .ima frame data multiplied by the exposure time of 7.35 seconds. A
186 wavelength calibration based on band filter observations and the WFC3 dispersion
187 relation results in an uncertainty of 5 nm/pixel. The eclipse depth in individual channels
188 is estimated by a joint simultaneous fit to a model light curve and a linear trend in time
189 that spans orbits 2 to 5 (see Figures 6 and 7), where the slope of the linear trend and the
190 depth parameters are the free parameters adjusted by the fitting process. The primary
191 eclipse light curve model was generated by a 4-parameter, non-linear, limb-darkening
192 model (Claret 2000, 2011); the limb-darkening parameters were wavelength independent
193 (for the H-band) and were fixed during the fitting process. The system ephemeris from
194 (Maciejewski et al. 2011) and stellar parameters were taken from Hebb et al. (2009). We
195 find an offset of 4.7 ± 1.7 minutes with respect to the T0 of a linear ephemeris prediction
196 (Maciejewski et al. 2011), where the standard deviation of individual spectral channels is
197 ± 0.1 minutes. Both the primary and secondary eclipse light curve models were generated
198 using Mandel and Agol (2002) algorithms. We estimated the eclipse depth uncertainty
199 using (1) the uncertainty as estimated by the multi-parameter (Levenberg-Marquadt type)
200 fitting process, (2) the MCMC method, (3) a prayer-bead style residual permutation
201 analysis, (4) and the standard deviation in the mean of the residual time series and find all

202 methods give results consistent results for these data (e.g., for the 1.3763- μm channel, the
203 uncertainties for these four methods are 179, 175, 178, and 170 ppm, respectively).

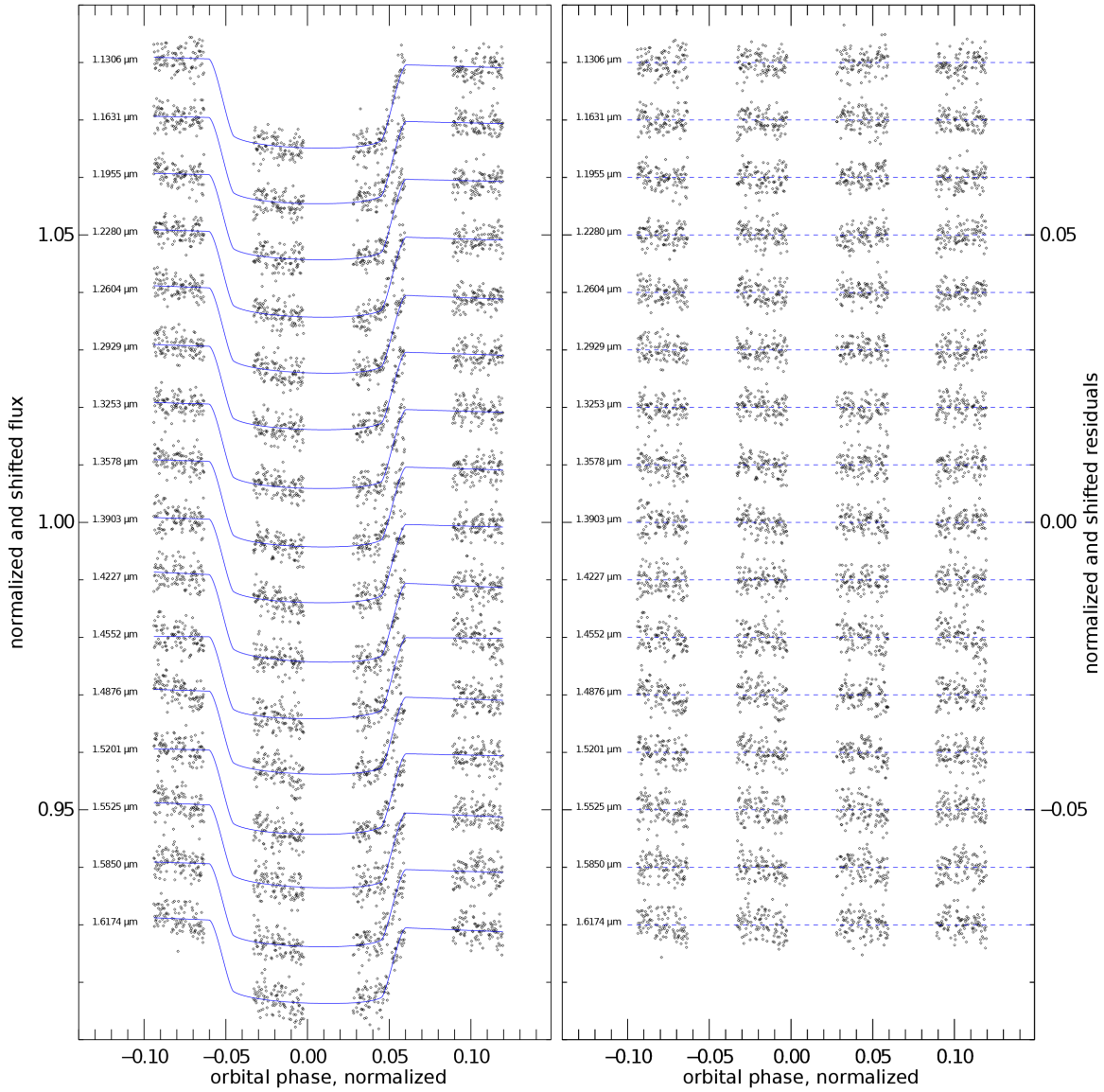


Figure 6: The primary eclipse measurements for each spectral channel together with the best fit model shown in blue (left) and model residuals (right).

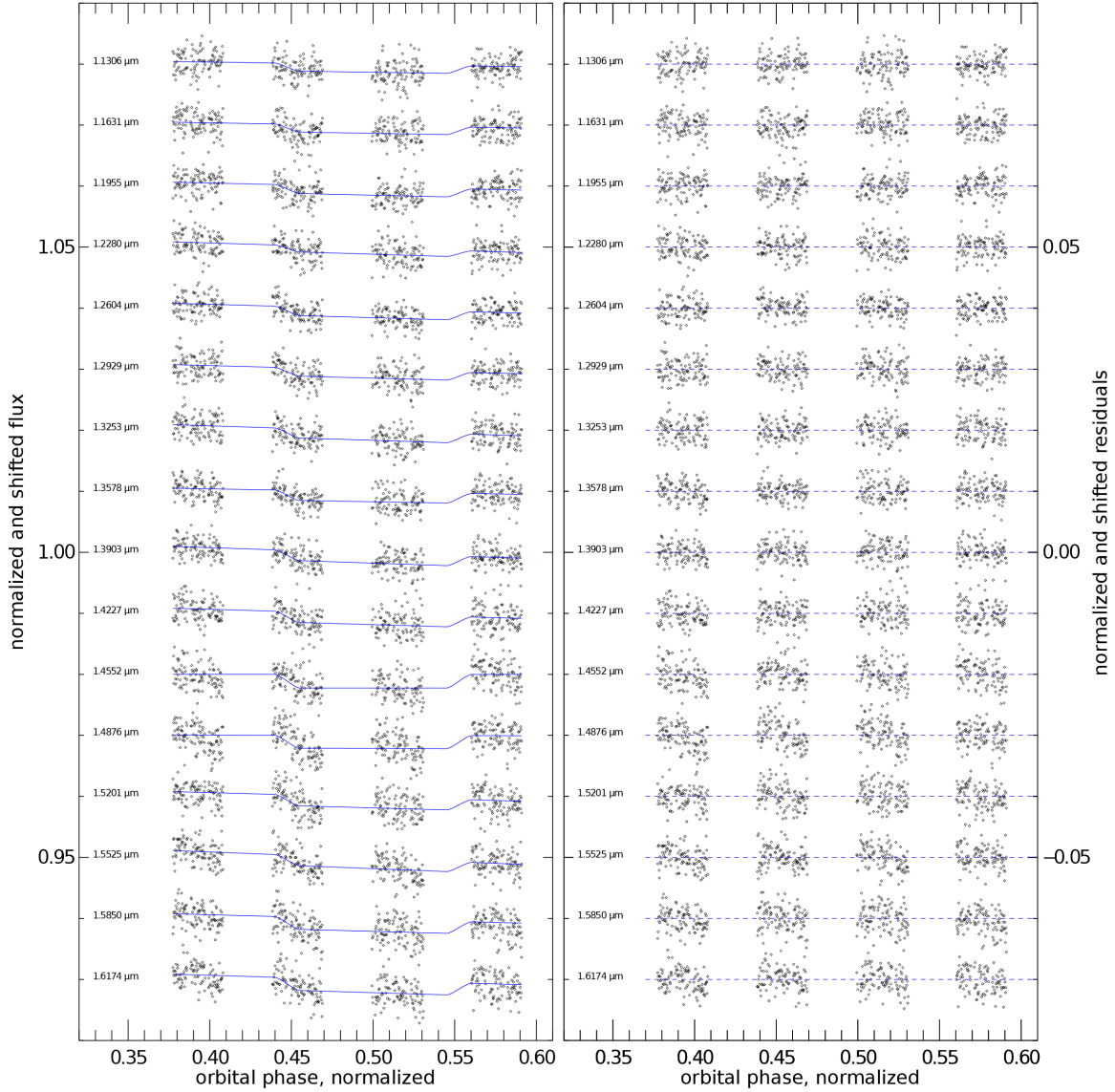


Figure 7: The secondary eclipse measurements for each spectral channel together with the best fit model shown in blue (left) and model residuals (right).

204 An additional correction needs to be considered in the case of WASP-12b. As noted
 205 by Crossfield et al. (2012b), the presence of a nearby star, identified as Bergfors-6,
 206 introduces an error in the measured eclipse depths. Bergfors-6 is visible in WFC3 narrow
 207 band filter images used for our wavelength calibration and detectable as an asymmetry in
 208 transverse profile of the WASP-12 system spectrum. Separation of the light from

209 Bergfors-6 from WASP-12 in our WFC3 data is possible, but requires some care. Using
 210 the spectroscopy observations of HD 258439, we determined the chromatic point spread
 211 function (PSF). The chromatic PSF was the used to fit two components — that of WASP-
 212 12 and Bergfors-6 — for each spectral channel (see Figure 8). This allowed a
 213 determination of the amount of light originating from Bergfors-6 and WASP-12b; both
 214 primary and secondary eclipse depths were then corrected, following the method of
 215 Kipping & Tinetti (2010), for the Bergfors-6 contamination.

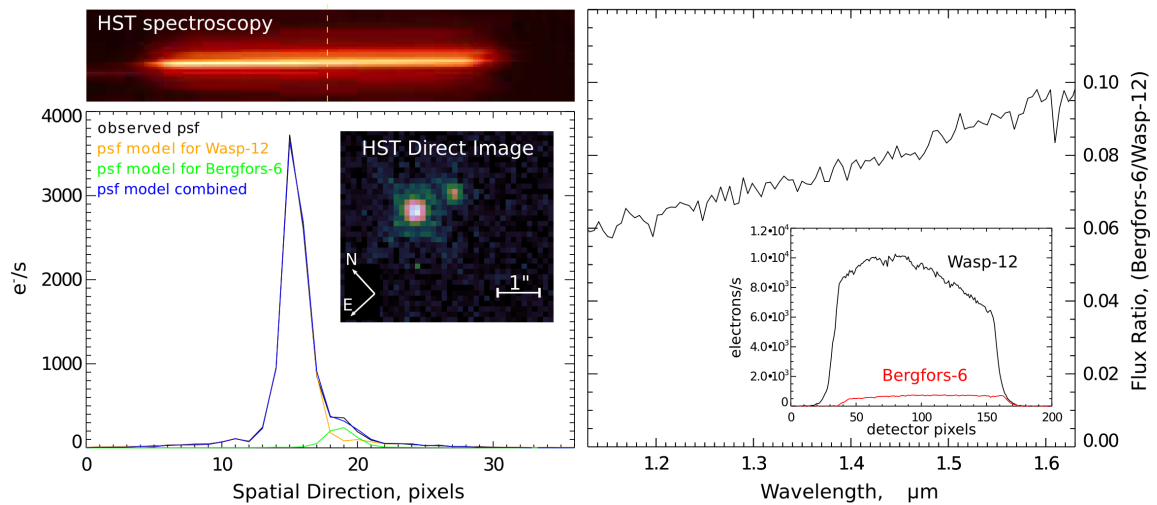


Figure 8: Left: The WFC3 spectrum WASP-12 includes a contribution from the nearby star Bergfors-6. The WFC3 direct image of WASP-12 clearly shows the fainter object Bergfors-6 located one arcsecond to the West. The contribution from Bergfors-6 to the WASP-12 spectrum is measured by fitting two PSF components to the transverse spectral profile. Right: The measured contribution of Bergfors-6 to the measurements allowing the WASP-12 component to be isolated.

216 To assess the quality of the linear inter-orbit detrending method, we compared the
 217 measured noise to the theoretical photon noise as a function of the number of spectral
 218 channels averaged to create the time series. This analysis shows that the detector behaves
 219 very well in this readout mode; the presence of systemic noise becomes detectable when

220 5 or more pixels are averaged together, but the systematic noise averages (see Figure 9)
221 down as pixels to the -0.4 power (-0.5 would be ideal). The signal-to-noise of the final
222 WASP-12b spectrum is increased by averaging together seven individual channels
223 weighted by the uncertainties and achieves about 160 ppm or ~ 1.15 times photon noise
224 (see Figure 10 and Table 2) and avoids the kinds of questions associated with complex
225 decorrelation methods. Recently, WFC3-IR measurements of an exoplanet transmission
226 spectrum have been reported by Berta et al. (2011) using an approach termed the OOT
227 method to remove the large intra-orbit systematics found in 512×512 subarray data. As a
228 consistency check, we applied the OOT method to our WASP-12 data and find virtually
229 identical results.

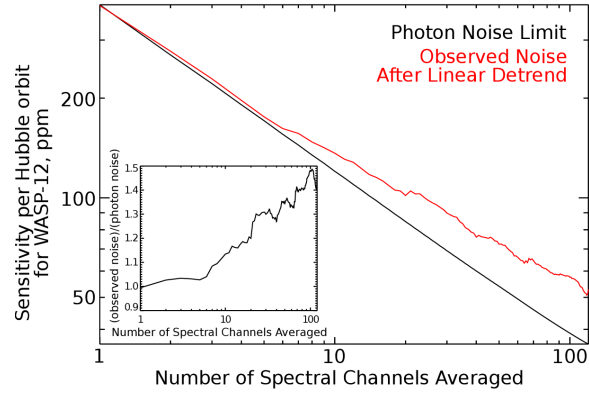


Figure 9: The excellent performance of WFC3 is shown by a comparison of the theoretical photon-limited noise, based on detected photons, and the standard deviation of residuals for the primary eclipse measurements using a single HST orbit centered on orbital phase -0.02 (see Figure 1) as a function of the number of pixel-based spectral channels averaged together. Instrument systematics become detectable when 5 or more pixel-based spectral channels are averaged together. However, these instrument systematic errors average down very well (only slightly worse than the square root of bandwidth) and the ultimate performance of the instrument is ~ 1.45 times the photon noise for our observations.

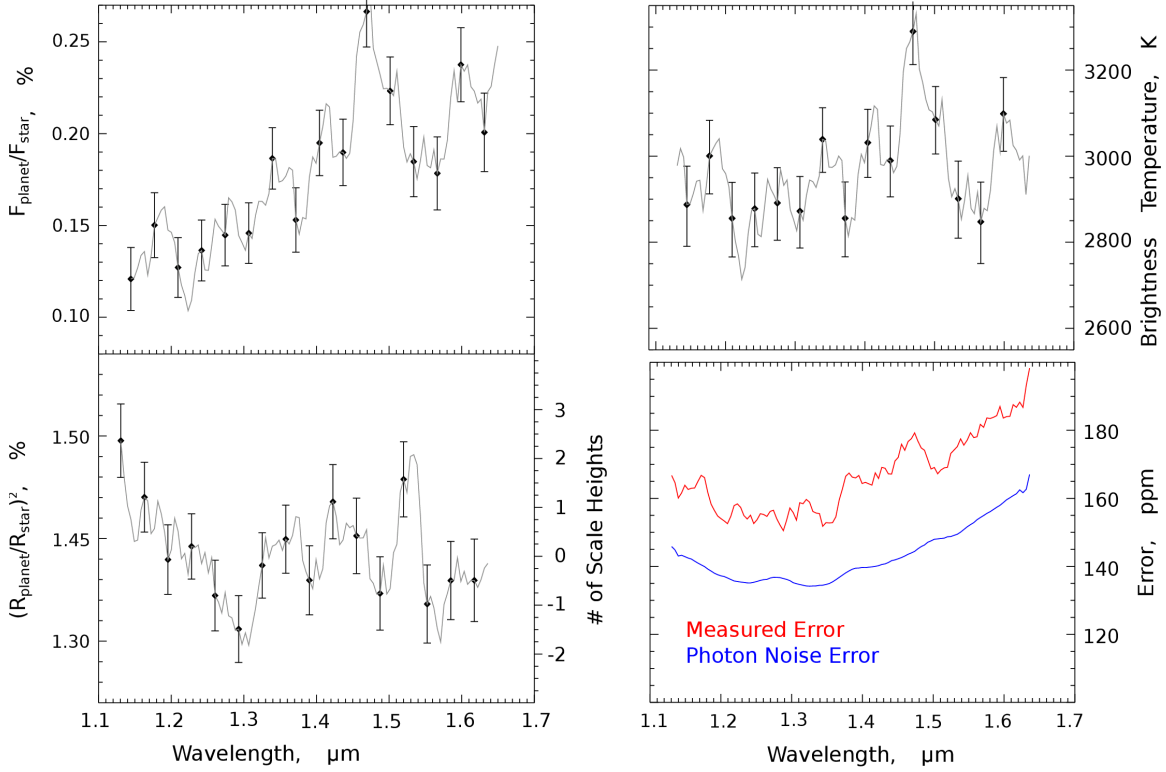


Figure 10: (Left) Dayside region emission spectrum (top) and terminator region transmission spectrum (bottom). The data averaged in the spectral dimension and statistically independent measurements are shown as solid circles with plus/minus $1\text{-}\sigma$ errors. The grey line shows the spectrum value computed using a scrolling boxcar. (Right) The dayside emission spectrum in units of brightness temperature (top) and an uncertainty spectrum showing how each channel compares to the photon noise (bottom). These measurements approach the theoretical limit for what is achievable with WFC3 in the IR grism spectroscopy mode.

230 For a measurement precision of ~ 160 ppm, corresponding to averaging 7 pixel-based
 231 spectral channels together in these observations, the 256×256 subarray mode delivers
 232 nearly ideal noise properties. When the entire 120-pixel passband is averaged together,
 233 the measured noise of ~ 52 ppm is about 1.45 times the theoretical instrument precision
 234 (see Figure 9). This shows that WFC3 IR is a very good instrument for exoplanet
 235 characterization. Instrument systematic errors are present, but they average down

236 relatively well. Two separate instrument systematics become detectable in the WASP-
237 12b data when the entire spectral passband is averaged together. The first of these
238 systematics is an intra-orbit, linear flux change that is easily detrended based on the out-
239 of-eclipse data. The second of these systematics is a pattern in the data for each orbit
240 associated with the third (and final) buffer dump; these data have a systematically lower
241 flux value that becomes apparent when averaging the data together for the entire
242 passband. Attempts to decorrelate using the optical state vectors did not work, but an
243 OOT style of approach should prove effective. We did not pursue further correction of
244 this particular systematic because it does not interact with the science related analysis for
245 this paper. Additional observations of both science targets and calibrator stars would
246 benefit our understanding of the ultimate dynamic range capabilities of the instrument.

247 From the point of view of extracting a spectrum of WASP-12b with spectral
248 resolution of $\Delta\lambda/\lambda = 42$, corresponding to averaging 7 pixel-based spectral channels, the
249 measurement noise budget can be modeled as the root sum of squares of several
250 components. Selecting 1.38 μm for the reference wavelength, we model the uncertainty
251 as 140 ppm due to photon shot noise, 16.5 ppm due to electronics noise, 65 ppm due to a
252 systematic component that is wavelength independent, and 55 ppm due to a systematic
253 that is wavelength dependent and affects the 1.38-1.48 μm channels (see Figure 10). This
254 model is a worst case scenario and assumes the systematic errors have a covariance of
255 zero; if this is not the case, the amplitude of the one or both of the systematic error terms
256 is reduced to accommodate the covariance contribution. Given that (1) a calibration
257 method based on a linear detrending of inter-orbit data results in a measurement error that
258 is within 15% of the theoretical limit, (2) we wish to avoid the debate associated with

259 more complex systematic error removal, and (3) our measurement uncertainties
 260 incorporate the affect of the small residual systematic errors, we proceed with the science
 261 analysis using the calibration based on the simple linear detrending of the inter-orbit data.

Table 2: *The transmission and emission spectrum data determined as described in Section 2.3. The values represent the average of seven pixel-based spectral channels; thus, every seventh wavelength is a statistically independent sample, and there are seven equally valid wavelength grids. The error estimate is derived from a combination of the multiparameter fitting process and the uncertainty in the removal of the Bergfors-6 emission. Data for the wavelength grid we use for plotting the spectra begins with 1.1306 μm and is every seventh row thereafter.*

Transmission Spectrum			Emission Spectrum		
λ [μm]	$(R_p/R_s)^2$ [%]	1- σ error [%]	λ [μm]	F_p/F_s [ppm]	1- σ error [ppm]
1.1306	1.498	0.018	1.1306	1355	177
1.1353	1.480	0.018	1.1353	1440	174
1.1399	1.466	0.017	1.1399	1411	170
1.1445	1.459	0.017	1.1445	1208	171
1.1492	1.449	0.017	1.1492	1216	174
1.1538	1.449	0.016	1.1538	1269	172
1.1584	1.464	0.017	1.1584	1336	173
1.1631	1.470	0.017	1.1631	1357	173
1.1677	1.468	0.017	1.1677	1229	175
1.1723	1.452	0.018	1.1723	1335	177
1.1770	1.455	0.018	1.1770	1501	177
1.1816	1.468	0.018	1.1816	1541	172
1.1863	1.462	0.018	1.1863	1582	168
1.1909	1.453	0.017	1.1909	1601	166
1.1955	1.440	0.017	1.1955	1474	164
1.2002	1.445	0.017	1.2002	1462	164
1.2048	1.460	0.017	1.2048	1406	163
1.2094	1.454	0.017	1.2094	1270	162
1.2141	1.440	0.016	1.2141	1175	165
1.2187	1.443	0.016	1.2187	1118	168
1.2233	1.433	0.016	1.2233	1035	169
1.2280	1.446	0.016	1.2280	1091	168
1.2326	1.446	0.016	1.2326	1241	165
1.2373	1.447	0.016	1.2373	1346	164
1.2419	1.438	0.016	1.2419	1363	165
1.2465	1.443	0.017	1.2465	1257	163

Table 2: The transmission and emission spectrum data determined as described in Section 2.3.

The values represent the average of seven pixel-based spectral channels; thus, every seventh wavelength is a statistically independent sample, and there are seven equally valid wavelength grids. The error estimate is derived from a combination of the multiparameter fitting process and the uncertainty in the removal of the Bergfors-6 emission. Data for the wavelength grid we use for plotting the spectra begins with 1.1306 μm and is every seventh row thereafter.

Transmission Spectrum			Emission Spectrum		
λ [μm]	$(R_p/R_s)^2$ [%]	1- σ error [%]	λ [μm]	F_p/F_s [ppm]	1- σ error [ppm]
1.2512	1.433	0.017	1.2512	1255	164
1.2558	1.441	0.017	1.2558	1390	166
1.2604	1.422	0.017	1.2604	1533	166
1.2651	1.419	0.017	1.2651	1495	165
1.2697	1.414	0.017	1.2697	1472	167
1.2743	1.424	0.017	1.2743	1447	167
1.2790	1.412	0.017	1.2790	1650	165
1.2836	1.411	0.017	1.2836	1629	163
1.2883	1.405	0.017	1.2883	1583	161
1.2929	1.406	0.016	1.2929	1444	164
1.2975	1.398	0.016	1.2975	1406	168
1.3022	1.404	0.016	1.3022	1364	167
1.3068	1.398	0.016	1.3068	1458	164
1.3114	1.407	0.016	1.3114	1428	170
1.3161	1.416	0.016	1.3161	1554	170
1.3207	1.427	0.016	1.3207	1631	171
1.3253	1.437	0.016	1.3253	1630	170
1.3300	1.450	0.016	1.3300	1610	167
1.3346	1.441	0.016	1.3346	1673	167
1.3393	1.446	0.016	1.3393	1865	167
1.3439	1.447	0.016	1.3439	1860	163
1.3485	1.449	0.017	1.3485	1736	164
1.3532	1.444	0.017	1.3532	1743	164
1.3578	1.450	0.017	1.3578	1768	164
1.3624	1.447	0.016	1.3624	1815	166
1.3671	1.452	0.016	1.3671	1800	171
1.3717	1.461	0.016	1.3717	1529	175
1.3763	1.460	0.016	1.3763	1452	179
1.3810	1.439	0.017	1.3810	1542	180
1.3856	1.434	0.017	1.3856	1535	179
1.3903	1.430	0.017	1.3903	1763	179
1.3949	1.426	0.017	1.3949	1873	180

Table 2: The transmission and emission spectrum data determined as described in Section 2.3.

The values represent the average of seven pixel-based spectral channels; thus, every seventh wavelength is a statistically independent sample, and there are seven equally valid wavelength grids. The error estimate is derived from a combination of the multiparameter fitting process and the uncertainty in the removal of the Bergfors-6 emission. Data for the wavelength grid we use for plotting the spectra begins with 1.1306 μm and is every seventh row thereafter.

Transmission Spectrum			Emission Spectrum		
λ [μm]	$(R_p/R_s)^2$ [%]	1- σ error [%]	λ [μm]	F_p/F_s [ppm]	1- σ error [ppm]
1.3995	1.440	0.017	1.3995	1838	177
1.4042	1.430	0.018	1.4042	1949	178
1.4088	1.435	0.018	1.4088	2037	177
1.4134	1.458	0.018	1.4134	2162	177
1.4181	1.466	0.018	1.4181	2144	181
1.4227	1.468	0.018	1.4227	1871	179
1.4273	1.461	0.018	1.4273	1876	183
1.4320	1.447	0.018	1.4320	1901	182
1.4366	1.449	0.018	1.4366	1897	181
1.4412	1.458	0.019	1.4412	1865	181
1.4459	1.455	0.019	1.4459	1892	185
1.4505	1.456	0.019	1.4505	2068	186
1.4552	1.451	0.018	1.4552	2420	190
1.4598	1.450	0.019	1.4598	2553	189
1.4644	1.450	0.018	1.4644	2593	191
1.4691	1.454	0.018	1.4691	2664	192
1.4737	1.430	0.018	1.4737	2785	194
1.4783	1.428	0.018	1.4783	2464	192
1.4830	1.423	0.018	1.4830	2393	190
1.4876	1.423	0.018	1.4876	2322	189
1.4922	1.437	0.018	1.4922	2244	186
1.4969	1.423	0.018	1.4969	2246	183
1.5015	1.426	0.018	1.5015	2232	184
1.5062	1.443	0.018	1.5062	2206	182
1.5108	1.447	0.018	1.5108	2339	183
1.5154	1.473	0.018	1.5154	2132	184
1.5201	1.479	0.018	1.5201	1927	184
1.5247	1.473	0.018	1.5247	1845	189
1.5293	1.490	0.019	1.5293	1890	190
1.5340	1.491	0.019	1.5340	1847	191
1.5386	1.486	0.019	1.5386	1753	193
1.5432	1.461	0.019	1.5432	1852	192

Table 2: The transmission and emission spectrum data determined as described in Section 2.3. The values represent the average of seven pixel-based spectral channels; thus, every seventh wavelength is a statistically independent sample, and there are seven equally valid wavelength grids. The error estimate is derived from a combination of the multiparameter fitting process and the uncertainty in the removal of the Bergfors-6 emission. Data for the wavelength grid we use for plotting the spectra begins with 1.1306 μm and is every seventh row thereafter.

Transmission Spectrum			Emission Spectrum		
λ [μm]	$(R_p/R_s)^2$ [%]	1- σ error [%]	λ [μm]	F_p/F_s [ppm]	1- σ error [ppm]
1.5479	1.428	0.019	1.5479	1981	193
1.5525	1.418	0.019	1.5525	1826	196
1.5572	1.422	0.019	1.5572	1814	194
1.5618	1.416	0.019	1.5618	1911	194
1.5664	1.406	0.019	1.5664	1783	198
1.5711	1.400	0.019	1.5711	1862	198
1.5757	1.418	0.019	1.5757	1861	201
1.5803	1.423	0.019	1.5803	1963	201
1.5850	1.430	0.019	1.5850	2198	201
1.5896	1.430	0.019	1.5896	2342	202
1.5942	1.441	0.020	1.5942	2172	205
1.5989	1.429	0.020	1.5989	2375	201
1.6035	1.434	0.020	1.6035	2340	202
1.6082	1.428	0.020	1.6082	2374	202
1.6128	1.430	0.020	1.6128	2255	206
1.6174	1.430	0.020	1.6174	2231	205
1.6221	1.426	0.020	1.6221	2166	207
1.6267	1.430	0.020	1.6267	2187	205
1.6313	1.436	0.020	1.6313	2006	213
1.6360	1.438	0.021	1.6360	2229	220

263 Determining the depth of the primary and secondary eclipse, as a function of
264 wavelength, provides different physical insights into the planetary atmosphere. For the
265 primary eclipse, the depth is a measurement of $(R_p/R_s)^2$ where R_p is the radius of the
266 planet and R_s is the radius of the parent star. For the secondary eclipse measurement, the
267 depth is the ratio of $F_p/(F_s + F_p) \sim F_p/F_s$, where F_p is the flux density of the primary and
268 F_s is the flux density of the parent star. In addition to working with these parameters, we
269 find it useful to represent the primary eclipse (transmission) spectrum in units of scale
270 height and the secondary eclipse (emission) spectrum in units of brightness temperature
271 (Figure 10); for calculating the brightness temperature, we use a model for WASP-12
272 (Castelli & Kurucz 2003). To provide context, we compare WASP-12b to the only two
273 other hot-Jupiter class planets with near-infrared emission spectra measured with HST
274 (see Figure 11 and Table 3).

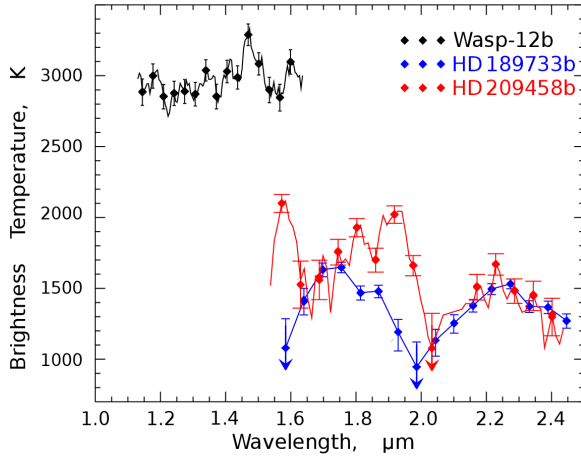


Figure 11: (Left) Brightness temperature spectra for the three hot-Jovians with emission spectra measured by HST. (Right) Placing WASP-12 in context.

Table 3: Assumptions for this calculation include a Bond albedo = 0.00, Internal energy = 0.00, Molecular weight = 2, and perfect heat redistribution. Differences between the planet temperature estimate in this table and the measured brightness temperature are due to these assumptions.

275 3. Atmospheric Modeling

276 We explored constraints provided by the spectral time series for the composition of
 277 the terminator region atmosphere, the composition and temperature structure of the
 278 dayside atmosphere, and the spatial distribution of dayside flux density. Interpreting
 279 exoplanet spectra via models is the norm in the field. The approaches we used have been
 280 discussed in previous work. Specifically, we use two Bayesian retrieval approaches to
 281 analyze both the transmission and emission spectra. The first approach, the optimal
 282 estimation approach (Lee et al. 2011, Line et al. 2012), determines the best fit
 283 compositions and temperatures by minimizing a quadratic (reduced χ^2) cost function. To

284 determine the uniqueness of the solution, multiple initial composition and temperature
285 guesses are used. To account for non-Gaussian errors (specifically, upper limits), we use
286 the MCMC retrieval approach (Madhusudhan & Seager 2009, Benneke & Seager 2012).
287 The forward model for the emission spectra solves the thermal infrared radiative transfer
288 equation over 90 levels evenly spaced in logP between 30 bars and 1E-6 bars. The
289 transmission forward model solves the limb transmittance radiative transfer equation over
290 45 atmospheric layers evenly spaced in logP between 10 bars and 1E-10 bars. Both
291 models use the HiTemp (Rothman et al. 2010) database for H₂O, CO, and CO₂, the STDS
292 database (Wenger et al. 1998) for CH₄, and the Sharp & Burrows 2007 database for TiO
293 and VO, along with H₂-H₂/He CIA opacity from Borysow et al. 2001, 2002. We compare
294 emission and transmission models quantitatively using three factors:

- 295 1. The reduced χ^2 ; that is, of χ^2 divided by the total number of data points. Values of
296 1 suggest that the model fits are generally within 1-sigma of the data errors.
- 297 2. The degrees of freedom (DOF), which is the total number of independent pieces
298 of information that can be obtained from the data, as defined by Rodgers 2000.
299 This is not the same as the total number of free parameters. In fact, our definition
300 of DOF often leads to a lesser value than the total number of free parameters,
301 suggesting that not all parameters can be constrained. The DOF is computed from
302 the averaging kernel described in Line et al. 2012.
- 303 3. The Bayesian Information Criterion (BIC), which is the $\chi^2 + k \ln(n)$. k is the total
304 number of free parameters and n is the total number of data points. When the total
305 number of parameters increase, a better fit can be obtained, which reduces χ^2 ;
306 however, the BIC is penalized for those additional parameters. Models with

307 lower BICs are preferred. The addition of a model parameter can only be justified
308 if it improves the fit quality more than the penalization from adding that
309 additional parameter.

310 **4. Results**

311 While the primary and secondary eclipse measurements probe separate atmospheric
312 regions and were modeled individually, we used atmospheric “cases” with identical
313 opacity sources for both the primary and secondary eclipse data to provide a uniform
314 basis for comparison. The atmospheric opacity cases span a range from pure H₂
315 continuum opacity to a more physically motivated atmosphere containing H₂O, CH₄, CO,
316 CO₂, TiO, and VO. We consider both the WFC3 measurements and Spitzer photometry
317 measurements (Madhusudhan et al. 2011a; Cowen et al. 2012), and the atmospheric
318 models (see Figure 12 and 13) are compared on the basis of goodness of fit and the BIC
319 (see Table 4). Two noteworthy conclusions result from comparing the models. First, on
320 the basis of the existing data, we find no support for including opacity sources beyond H₂
321 continuum. Second, even when we include additional molecular opacity, we find no
322 evidence to support a conclusion of C/O > 1. If anything, the modeling suggests that the
323 atmosphere is C depleted.

324 We stress that these results are indicational due to the limited spectral coverage
325 available. The modeling shows that an improved understanding of the WASP-12b
326 atmosphere requires spectroscopic observations over a larger range of wavelengths. We
327 explored inclusion of TiH and CrH for opacity sources and find that they can be
328 consistent with the data; this exploration was undertaken using the iterative forward
329 model approach with an implementation described by Tinetti et al. (2007a) and

330 subsequently refined in terms of line lists adopted (Tinetti et al. 2007b, Tinetti et al. 2010,
331 Burrows et al. 2005, Burrows et al. 2002). Although TiH and CrH may be consistent with
332 the WFC3 data, we have not undertaken the detailed thermal-chemical modeling that
333 would justify specific selection of these particular metal hydrides given that other
334 possibilities also exist (Sharp & Burrows, 2007). We also note that inclusion of a model
335 for the atmospheric response may be needed to connect the dayside and terminator
336 regions conditions in a detailed way. Despite these limitations, our preliminary modeling
337 is able to provide some insight into the atmosphere of WASP-12b. What emerges is a
338 picture of an exoplanet atmosphere that is like no other exoplanet characterized with
339 infrared spectroscopy to date.

340 **4.1 Terminator Region**

341 The terminator region transmission spectrum of WASP-12b shows maximum opacity
342 at short wavelengths, dropping to a local minimum at 1.3 μm . Additional opacity
343 structure between 1.30 and 1.55 μm is adjacent to the region of minimal opacity between
344 1.56 and 1.64 μm . The opacity slope between 1.1 and 1.3 μm is especially noteworthy.
345 This feature corresponds to about 3 atmospheric scale heights (see Figure 10). While the
346 slope is suggestive of scattering due to dust or aerosols, the slope is too steep to explain
347 in this manner alone. We find that models with H₂O, TiO, and VO partially explain this
348 feature, while the H₂ continuum and H₂O/CH₄/CO/CO₂ models show significant
349 departures from the data in this region (see Figure 12). Although the H₂ continuum
350 transmission model has the lowest BIC, the inclusion H₂O/TiO/VO is favored over
351 H₂O/CH₄/CO/CO₂ based on the combination of χ^2 and BIC values.

352 **4.2 Dayside Emission**

353 What immediately stands out in the dayside emission spectrum of WASP-12b is the
354 extremely high brightness temperature of this atmosphere. In the near-infrared, the
355 typical brightness temperature is about 2900 K. The minimum brightness temperature is
356 about 2700 K at 1.22 μm , and the maximum brightness temperature is 3200 K at 1.47 μm .
357 As with the transmission spectrum, an atmospheric-emission model based on H_2 , with no
358 additional sources of opacity, is preferred by a BIC selection criteria. Unlike the
359 transmission spectrum, if additional opacity sources are added, $\text{H}_2\text{O}/\text{CH}_4/\text{CO}/\text{CO}_2$ are
360 favored over $\text{H}_2\text{O}/\text{TiO}/\text{VO}$ based on a combination of χ^2 and BIC values (see Figure 12).
361 For the $\text{H}_2\text{O}/\text{CH}_4/\text{CO}/\text{CO}_2$ opacity-based model, we find abundances consistent with an
362 elemental ratio of $\text{C}/\text{O} < 1$. We also find no evidence for a temperature inversion (see
363 Figure 13). Our result that the model with the most favorable BIC is based on H_2
364 continuum, with no additional opacity, supports the recent findings by Crossfield et al.
365 (2012b), who argue that more complex models are not supported by the data. If we
366 include opacity due to $\text{H}_2\text{O}/\text{CH}_4/\text{CO}/\text{CO}_2$, our results disagree with the finding of
367 Madhusudhan et al. (2011a) reporting the $\text{C}/\text{O} > 1$.

Table 4: A summary of the opacity sources used to model both the dayside emission and terminator region transmission spectra showing the comparison of the models with the data using the χ^2 and BIC together with retrieved molecular abundance values for each case.

case		transmission		emission		
Case 1	C/O	$\chi^2=2.63$	-	C/O	$\chi^2=4.24$	-
	-	DoF=1.07	-	-	DoF=1.95	-
		BIC=14.2	-		BIC=19.7	-
Case 2	C/O	$\chi^2=2.59$	H ₂ O=1.91E-4	C/O	$\chi^2=2.64$	H ₂ O=3.96E-8
	1.6E-2	DoF=2.02	CH ₄ =9.58E-12	6.6E-1	DoF=3.33	CH ₄ =6.32E-7
		BIC=25.7	CO=3.32E-7		BIC=30.5	CO=8.60E-7
			CO ₂ =2.90E-6			CO ₂ =2.73E-6
Case 3	C/O	$\chi^2=1.50$	H ₂ O=6.32E-5	C/O	$\chi^2=4.07$	H ₂ O=7.90E-8
	-	DoF=3.18	TiO=4.15E-5	-	DoF=4.32	TiO=3.23E-6
		BIC=21.7	VO=3.97E-5		BIC=28.8	VO=8.79E-6
Case 4	C/O	$\chi^2=1.48$	H ₂ O=1.17E-4	C/O	$\chi^2=2.36$	H ₂ O=3.44E-8
	1.3E-3		CH ₄ =2.25E-8	2.9E-1		CH ₄ =8.18E-7
		DoF=3.37	CO=2.36E-7		DoF=5.38	CO=7.98E-7
			CO ₂ =2.00E-8			CO ₂ =5.78E-6
		BIC=30.4	TiO=5.23E-5		BIC=36.4	TiO=1.30E-5
		VO=5.07E-5			VO=1.30E-5	

Results of Uncertainty Analysis for Atmospheric Retrievals				
molecule	Emission Spectra Abundances		Transmission spectra abundances	
	uncertainty	constraint	uncertainty	constraint
H2O	4.65E-14 - 2.8E-02	0.04-poor	1.57E-05 - 8.65E-04	0.95-good
CH4	8.95E-08 - 6.12E-06	0.98-good	3.15E-12 - 1.61E-04	0.07 - poor
CO	1.14E-12 - 5.67E-01	0.05-poor	2.47E-11 - 2.26E-03	0.01 -poor
CO2	7.04E-09 - 2.40E-03	0.79-limited	4.81E-12 - 8.34E-05	0.18-poor
TiO	2.42E-06 - 6.13E-05	0.98-good	6.43E-06 - 4.25E-04	0.95--good
VO	3.08E-06 - 4.96E-05	0.99 -good	5.07E-06 - 5.06E-04	0.97--good

Terminator Transmission Models Dayside Emission Spectrum models

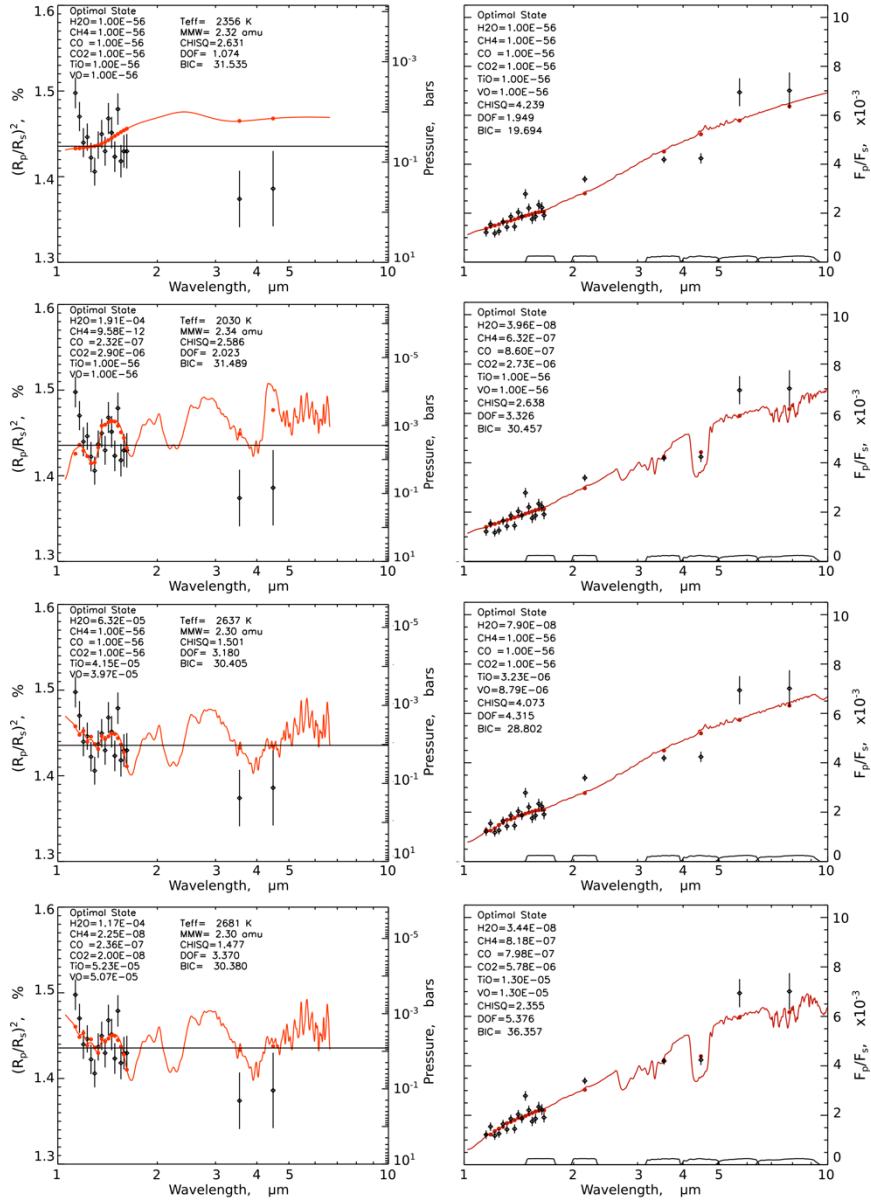


Figure 12: Data and best fitting models for the dayside emission (left) and terminator region transmission (right) considering four opacity scenarios listed in Table 4. The model based on H_2 with no additional opacity sources has the lowest BIC, implying that more observational data is needed to constrain the presence of additional opacity sources. Molecular abundance and model parameters are listed as inset text for each scenario.

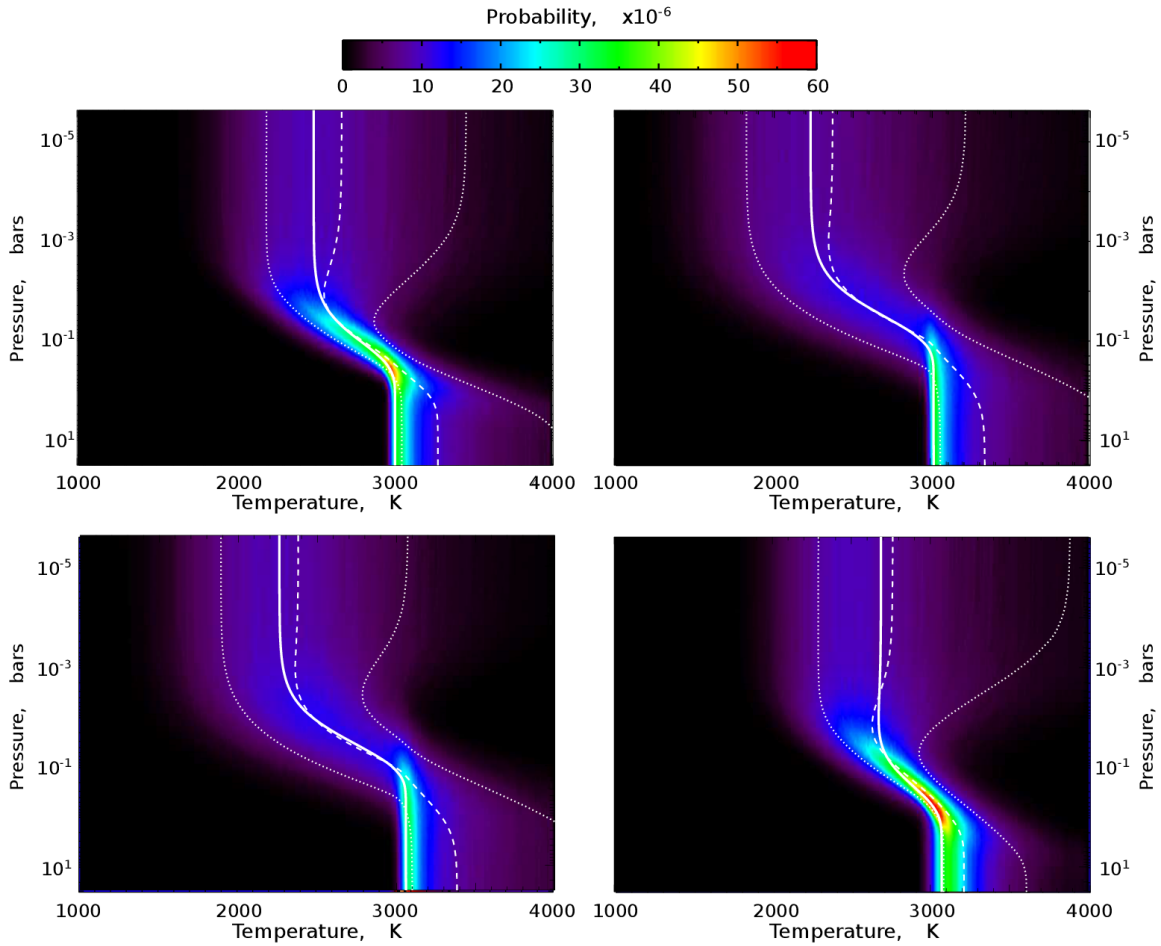


Figure 13: Temperature profiles retrieved for each of the four dayside atmosphere cases listed in Table 4, with case 1 in the upper left location and moving clockwise for the other cases. The solid line is the "best-fit" temperature profile and the two dotted curves are the ± 1 sigma. The dashed curve in the middle is the "median" temperature given all of the degeneracies amongst the temperature parameters and gasses.

369 **Discussion:**

370 This is the first time that high fidelity, space-based spectroscopy of a planet this hot
371 has been obtained. The spectra of the terminator and dayside regions are separated by
372 28.4 hours and come as close to taking a spectral “snap-shot” of the planet’s atmosphere
373 as is observationally possible with HST. An advantage of temporally closely spaced
374 observations is that they minimize the potential for stellar variations or climate variability
375 in the exoplanet. Although we treated these regions separately in our modeling effort, we
376 were able to find that an H₂ atmosphere, with no additional opacity sources, is the
377 optimal using a BIC criterion. If additional opacity source are present, we find no
378 evidence for C/O>1 and, thus, simultaneously confirm the findings of Crossfield et al.
379 (2012b) and differ from the findings of Madhusudhan et al. (2011a). In cases where
380 additional molecular opacity was added, we found that CO, TiO, and VO tended to have
381 similar abundance solutions for emission and transmission spectra, whereas H₂O and CH₄
382 tended to have substantially different dayside and terminator abundances; the behavior of
383 CO₂ was in between these two extremes. While the pure H₂ atmosphere is preferred in
384 some sense by the data, a more physically plausible atmosphere is likely to contain some
385 molecules. Our modeling shows that the pressure scale probed by these observations is
386 uncertain and will remain so until the atmospheric composition can be better constrained
387 either through additional data or detailed modeling.

388 The dayside brightness temperature of WASP-12b is sufficiently high that it is the
389 same as the temperature of red dwarf stars of M4V to M5V class and, thus, represents an
390 extreme case of the hot-Jovian class exoplanets. Only two other hot-Jovian type planets
391 have had HST measurements of the near-infrared emission spectrum, and they have

392 significantly lower near-IR brightness temperatures than WASP-12b (see Figure 11).
393 Given the extreme nature of the WASP-12b atmosphere, perhaps it is not surprising that
394 opacity due to TiO, VO and also TiH and CrH may be compatible with the data. Because
395 we do not undertake any thermo-chemical modeling, we consider our models to be
396 preliminary and accept they do not provide a complete view of the planet's atmosphere.
397 Opacity due to TiO/VO has been proposed (Hubeny et al. 2003, Fortney et al. 2008) as a
398 mechanism to produce temperature inversions in hot-Jovian type exoplanets. The
399 currently available data in the near-infrared and mid-infrared, are not sufficient to directly
400 constrain the opacity sources or the C/O ratio. Observations with improved spectral
401 coverage, and higher SNR, would likely provide the needed additional constraints to
402 dramatically improve our ability to understand the WASP-12b atmosphere.

403 The proposed prolate distortion of WASP-12b (Li et al. 2010) is, in principle,
404 observable in the primary eclipse light curve. The presence of a prolate distortion causes
405 the eclipse depth to be slightly deeper at the edges because the projected area of the
406 planet is increased slightly for angular displacements away from the eclipse center. Using
407 Spitzer primary eclipse measurements, Cowan et al. (2012) found indications of a larger
408 than predicted prolate distortion at measured 4.5 μm . Using our primary eclipse
409 measurements, we searched for the degree of prolate distortion consistent with the data
410 (see Figure 14). Our measurements, at the 95% confidence level, constrain the prolate
411 distortion to be less than 1.34 and are, thus, consistent with the degree of the prolate
412 distortion proposed by Li et al. (2010) and are inconsistent with the large values of
413 prolate distortion found by Cowan et al. (2012). This difference with the Cowen et al.
414 result could be due to probing different regions of the planetary atmosphere.

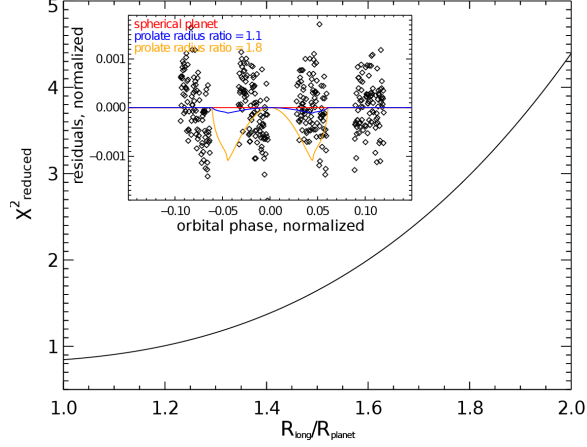


Figure 14: Results of a χ^2 analysis of the degree of prolate distortion consistent with the WFC3 data. The data are consistent with either a small degree of prolate distortion (including zero) while large degrees of prolate distortion are inconsistent with our measurements. Here, the degree of prolate distortion is measured by the ratio of radii of the planet along the axis pointing to the star, R_{long} , and the radii of the planet perpendicular to the star, R_{planet} .

415 **5. Conclusions**

416 We present WFC3-IR grism spectroscopy measurements of the dayside and
 417 terminator regions of WASP-12b. Our measurements show this is the hottest exoplanet
 418 thus characterized to date with a brightness temperature maximum of 3200 K. For both
 419 emission and transmission measurements, we find the atmospheric model with the lowest
 420 BIC is pure H_2 without additional opacity sources. We have explored more physically
 421 realistic model atmospheres containing a range of molecules and find no evidence of
 422 $C/O > 1$. This finding supports the results of Crossfield et al. 2012b and differs from the
 423 results of Madhusudhan et al. (2011a). We also find that TiH and CrH opacity is
 424 consistent with the WFC3 spectrum, suggesting that further investigation into sources of
 425 opacity in the atmospheres of very hot giant planets is desirable. From the standpoint of

426 temperature and opacity sources, the atmosphere of WASP-12b appears more star like
427 than planet like, confirming that this planet is truly an extreme world. These results,
428 together with previous observational and theoretical work, support the conclusion that
429 hot-Jupiter-type exoplanets are not a uniform class of objects and that these worlds
430 exhibit a diversity that we are only beginning to understand.

431 From an instrumental point of view, this paper reports the first exoplanet emission
432 spectrum measured with the WFC3 instrument. We also conducted a systematic analysis
433 of 65 orbits of WFC3-IR grism spectroscopy observation to characterize instrument
434 systematics. To our knowledge, the scope and detailed level of this instrument analysis is
435 unique in the area of exoplanet spectroscopy. We find that instrument systematics
436 originating in the detector system can vary considerably. The standard pipeline can mask
437 these problems, and we strongly encourage other researchers to analyze WFC3-IR
438 measurements at the individual non-destructive read (Nsamp) level. Notwithstanding the
439 problems with some detector modes, the WFC3 instrument is an excellent tool for
440 exoplanet spectroscopic characterization; when operated in the optimal detector readout
441 mode, WFC3-IR grism spectroscopy delivers nearly photon-noise-limited measurements
442 with a dynamic range of $\sim 6000:1$ that do not require complex decorrelation to correct
443 systematic errors.

444 **Acknowledgements:**

445 The research described in this publication was carried out in part at the Jet Propulsion
446 Laboratory, California Institute of Technology, under a contract with the National
447 Aeronautics and Space Administration. Y.F. and H.K are supported by JSPS (Japan
448 Society for the Promotion of Science) Fellowship for Research, DC:23-6070 and

449 PD:22-5467, respectively. We thank Nikku Madhusudhan for kindly providing the data
450 for a previously published theoretical model for comparison with these observations. We
451 are grateful to Rachel Akeson and Thomas Green for useful discussions and suggestions
452 on improving the manuscript. Copyright 2012. All rights reserved.

453 **References:**

454 Berta, Zachory K., et al., 2012. The Flat Transmission Spectrum of the Super-Earth
455 GJ1214b from Wide Field Camera 3 on the Hubble Space Telescope. *Astroph. J.*
456 747, 35B.

457 Benneke, B., Seager, S. 2012. Atmospheric Retrieval for Super-Earths: Uniquely
458 Constraining the Atmospheric Composition with Transmission Spectroscopy.
459 *Astroph. J.* 753, 100B.

460 Borysow, A., Jørgensen, U. G., & Fu, Y. 2001. High temperature (1000-7000K)
461 collision induced absorption of H₂ pairs computed from the first principles, with
462 application to cool and dense stellar atmospheres. *J. Quant. Spectrosc. Radiat.*
463 *Transfer*, 68, 235.

464 Borysow, A. 2002. Collision-induced absorption coefficients of H pairs at
465 temperatures from 60 K to 1000 K. *A&A*, 390, 779

466 Burrows A., Ram, R.S., Bernath, P., Sharp, C.M., Milsom, J.A., 2002. New CrH Opacities
467 for the Study of L and Brown Dwarf Atmospheres. *Astroph J.* 577,986.

468 Burrows, A., Dulick, M., Bauschlicher, C. W., Jr., Bernath, P. F., Ram, R. S., Sharp, C. M.,
469 Milsom, J. A., 2005. Spectroscopic Constants, Abundances, and Opacities of the TiH
470 Molecule. *Astroph. J.* 624, 988B.

471 Castelli, F. & Kurucz, R. L. 2003. New Grids of ATLAS9 Model Atmospheres. *AUS*,
472 210P, A20C.

473 Claret, A., 2000. A new non-linear limb-darkening law for LTE stellar atmosphere
474 models. Calculations for $-5.0 \leq \log[M/H] \leq +1$, $2000 \text{ K} \leq T_{\text{eff}} \leq 50000 \text{ K}$ at
475 several surface gravities. *A&A*, 406, 632C.

476 Claret, A., Bloemen, S., 2011. Gravity and limb-darkening coefficients for the Kepler,
477 CoRoT, Spitzer, uvby, UBVRIJHK, and Sloan photometric systems. *A&A*, 529, 75

478 Cowan, N. B., et al., 2012. Thermal Phase Variations of WASP-12b: Defying
479 Predictions. *Astroph. J.* 747,82C.

480 Croll, B., Lafreniere, D., Albert, L., Jayawardhana, R., Fortney, J., Murray, N., 2011.
481 Near-infrared Thermal Emission from WASP-12b: Detections of the Secondary
482 Eclipse in Ks, H, and J. *Astroph. J.* 141, 30C.

483 Crossfield, I. J. M., Hansen, B. M. S., Barman, T., 2012a. Ground-based, Near-infrared
484 Exospectroscopy. II. Tentative Detection of Emission from the Extremely Hot
485 Jupiter WASP-12b. *Astrphy. J.* 746, 46C.

486 Crossfield, I., Barman, T., Hansen, B., Tanaka, I., & Kodama, T. 2012b. Re-Evaluating
487 WASP-12b: Strong Emission at 2.315 micron, Deeper Occultations, and an
488 Isothermal Atmosphere. *arXiv*. 1210.4836C.

489 Fortney, J.J., Lodders, K., Marley, M.S., Freedman, R.S., 2008. A Unified Theory for the
490 Atmospheres of the Hot and Very Hot Jupiters: Two Classes of Irradiated
491 Atmospheres. *Astroph. J.* 678, 1419F.

492 Hebb, L., et al., 2009. WASP-12b: The Hottest Transiting Extra-solar Planet Yet
493 Discovered. *Astroph. J.* 693, 1920H.

494 Hubeny, I., Burrows, A., Sudarsky, D., 2003. A Possible Bifurcation in Atmospheres
495 of Strongly Irradiated Stars and Planets. *Astroph. J.* 594, 1011H.

496 Ibgui, L., Burrows, A., Spiegel, D., 2010. Tidal Heating Models for the Radii of the
497 Inflated Transiting Giant Planets WASP-4b, WASP-6b, WASP-12b, WASP-15b, and
498 TrES-4. *Astroph. J.* 713, 751I.

499 Kipping, D. & Tinetti, G. 2010. Nightside pollution of exoplanet transit depths.
500 *MNRAS.* 407, 2589K.

501 Lee, J.-M., Fletcher, L. N., Irwin, P. G. J. 2012. Optimal estimation retrievals of the
502 atmospheric structure and composition of HD 189733b from secondary eclipse
503 spectroscopy. *MNRAS.* 420, 170L.

504 Li, S., Miller, N., Lin, D. N. C., Fortney, J., 2010. WASP-12b as a prolate, inflated, and
505 disrupting planet from tidal dissipation. *Natur.* 463.1054L.

506 Line, M. R., Zhang, X., Vasisht, G., Natraj, V., Chen, P., Yung, Y. 2012. Information
507 Content of Exoplanetary Transit Spectra: An Initial Look. *Astroph. J.* 749, 93L.

508 Llama, J., Wood, K., Jardine, M., Vidotto, A. A., Helling, C., Fossati, L., Haswell, C., 2011.
509 The shocking transit of WASP-12b: modeling the observed early ingress in the
510 near-ultraviolet. 2011MNRAS. 416L, 41L.

511 Maciejewski, M., Errmann, R., Raetz, St., Seeliger, M., Spaleniak, I., Neuhauser, R.
512 2011. High-precision photometry of WASP-12 b transits. *A&A,* 528, 65M.

513 Madhusudhan, N., Seager, S. 2009. A Temperature and Abundance Retrieval Method
514 for Exoplanet Atmospheres. *Astroph. J.* 707, 24M.

515 Madhusudhan, N., et al., 2011a. A high C/O ratio and weak thermal inversion in the
516 atmosphere of exoplanet WASP-12b. *Natur.* 469, 64M.

517 Madhusudhan, N., Mousis, O., Johnson, T., Lunine, J., 2011b. Carbon-rich Giant
518 Planets: Atmospheric Chemistry, Thermal Inversions, Spectra, and Formation
519 Conditions. *Astroph. J.* 743, 191M.

520 Majeau, C., Agol, E., Cowan, N., 2012. A Two-dimensional Infrared Map of the
521 Extrasolar Planet HD 189733b. *Astroph. J.* 747L, 20M.

522 Pont, F., Gilliland, R. L., Knutson, H., Holman, M., Charbonneau, D., 2009. Transit
523 infrared spectroscopy of the hot Neptune around GJ 436 with the Hubble Space
524 Telescope. *MNRAS* 393, 6P.

525 Rothman, L. S., Gordon, I. E., Barber, R. J., et al. 2010, HITEMP, the high-temperature
526 molecular spectroscopic database. *J. Quant. Spectrosc. Radiat. Transfer*, 111, 2139.

527 Sharp, C. M., Burrows, A. 2007. Atomic and Molecular Opacities for Brown Dwarf and
528 Giant Planet Atmospheres. *Astrophs. J. Sup.* 168, 140S.

529 Swain, M. R., Vasisht, G., Tinetti, G., 2008. The presence of methane in the
530 atmosphere of an extrasolar planet. *Natur.* 452, 329S.

531 Swain, M. R., et al., 2009a. Molecular Signatures in the Near-Infrared Dayside
532 Spectrum of HD 189733b. *Astroph. J.* 609L,114S.

533 Swain, et al., 2009b. Water, Methane, and Carbon Dioxide Present in the Dayside
534 Spectrum of the Exoplanet HD 209458b. *Astroph. J.* 704,1616S.

535 Tinetti, G., Liang, M-C., Vidal-Madjar, A., Ehrenreich, D., Lecavelier des Etangs, A.,
536 Yung, Y. L., 2007a. Infrared Transmission Spectra for Extrasolar Giant Planets.
537 *Astroph. J.* 654, 99T.

538 Tinetti, G., et al., 2007b. Water Vapour in the atmosphere of a transiting extrasolar
539 planet. *Natur.* 448, 169T.

540 Tinetti, G., et al., 2010. Probing the Terminator Region Atmosphere of the Hot-
541 Jupiter XO-1b with Transmission Spectroscopy. *Astroph. J.* 712L, 139T.

542 Wenger, C., Champion, J.-P. 1998. Spherical top data system (STDS) software for the
543 simulation of spherical top spectra. *J. Quant. Spectrosc. Radiat. Transfer* 59,471-
544 480.

545 Zhao, M., Monnier, J. D., Swain, M. R., Barman, T., Hinkley, S., 1012. Ground-based
546 Detections of Thermal Emission from CoRoT-1b and WASP-12b. *Astroph. J.* 744,
547 122Z.